Measuring velocity from zero-offset data by image focusing analysis

Biondo Biondi

ABSTRACT

Migration velocity can be estimated from zero-offset data by analyzing focusing and defocusing of residual-migrated images. The accuracy of these velocity estimates is limited by the inherent ambiguity between velocity and reflector curvature. However, velocity resolution improves when reflectors with different curvatures are present, as demonstrated by simple synthetic examples. The application of the proposed method to zero-offset field data recorded in the New York harbor yields a velocity function that is consistent with available geologic information and clearly improves the focusing of the reflectors.

INTRODUCTION

In Biondi (2009) I presented a method to extract quantitative velocity information by analyzing the focusing and defocusing of seismic images. This method is based on the *image-focusing* semblance functional that simultaneously measures image coherency along the structural-dip axes and the aperture-angle axes. I also discussed the ambiguity between reflector curvature and velocity, and how reflector curvature may bias velocity estimates from image focusing. The method I presented has two important characteristics. First, it explicitly takes into account the relation between reflector curvature and velocity. Second, it provides velocity information from image focusing that is consistent with the velocity information that we routinely extract from migrated images by analyzing their coherency along the data offset or the reflection-aperture angle axes.

In this paper, I apply the new method to velocity estimation from zero-offset data. Zero-offset data represent the extreme case where there is no velocity information coming from data redundancy with offset. In this case, velocity-estimation methods can only rely on velocity information contained in the focusing of the image. Therefore, the ambiguity between reflector curvature and migration velocity can severely limit velocity resolution.

Tests on simple synthetic data sets illustrate the curvature-velocity ambiguity, but also demonstrate that velocity resolution increases as the range of reflector curvature broadens. These results are corroborated by the application of the method to zero-offset data acquired by a shallow-seismic survey in the New York harbor. I iteratively

update interval velocity in a sedimentary layer just below the water bottom. At each iteration, I estimate the value of residual-migration parameter that corresponds to the best focused image by evaluating the image-focusing semblance and picking its maximum. This value is then used to perform a conventional vertical interval-velocity update. The process converged after two iterations to an estimate of the sediment velocity that is consistent with available geologic information and improves the focusing of the migrated image.

IMAGE-FOCUSING VELOCITY ESTIMATION

In this section I briefly summarize the procedure I used to produce the results shown in the following two sections. The procedure is a simplification to zero-offset data of the method I presented in Biondi (2009).

The process starts from a partially-focused migrated image $\mathbf{R}(\mathbf{x})$, which is function of spatial coordinate vector $\mathbf{x} = \{z, x\}$, and continues with the following steps:

1. Perform residual migration on the initial image to produce an ensemble of residual-migrated images $\mathbf{R}(\mathbf{x}, \rho)$, where the parameter ρ is the ratio between the new migration velocity and the migration velocity used for the initial migration.

2. Estimate the local apparent structural dips in the residual-migrated images.

3. Dip-decompose the residual-migrated images, $\mathbf{R}(\mathbf{x}, \rho)$, to obtain the dip-decomposed images $\mathbf{R}(\mathbf{x}, \alpha, \rho)$, where α is the structural dip.

4. Perform the curvature correction (equation 2 in Biondi (2009)) of the dip-decomposed residual-migrated images, $\mathbf{R}(\mathbf{x}, \alpha, \rho)$, using the local-dip information extracted at step 2. The results of this process are the curvature-corrected images $\mathbf{R}_{\text{Curv}}(\mathbf{x}, \alpha, \rho, R)$, where R is the radius of curvature.

5. Compute image-focusing semblance as a function of ρ and R by applying the following equation,

$$S_\alpha(\mathbf{x}, \rho, R) = \frac{\left[\sum_\alpha \mathbf{R}_{\text{Curv}}(\mathbf{x}, \alpha, \rho, R)\right]^2}{N_\alpha \sum_\alpha \mathbf{R}_{\text{Curv}}(\mathbf{x}, \alpha, \rho, R)^2}, \tag{1}$$

   where N_α is the number of dips included in the semblance computation.

6. Average the semblance computed using equation 1 over a spatial analysis window, after clipping out the smallest values of the semblance to remove noise and artifacts.

To perform the residual migration listed in step 1 of the procedure outlined above I used the linearized residual migration described in the Appendix of Biondi (2008).

Other residual migration methods could be used, such as the one presented in Sava (2003). To simplify the analysis, I remapped the residual-migrated sections to pseudo-depth; that is, I remapped the depth axis of residual-migrated images according to the relationship $\tilde{z} = z/\rho$, where $\tilde{z}$ is pseudo-depth (Sava, 2004).

To estimate the local structural dips required by step 2, I used the Seplib program *Sdip* that implements a variant of the algorithms described by Fomel (2002). Any other local-dips estimator would be suitable. When performing the curvature correction at step 4, I define the curvature to be positive if the reflector frowns down (e.g. anticline) and negative if the reflector smiles up (e.g. syncline). The parameter N_α required for evaluating the focusing semblance at step 5 can be spatially varying according to the actual dip spectrum in the image. I kept it constant for my tests.

ZERO-OFFSET SYNTHETIC-DATA EXAMPLES

In this section, I present the application of the method outlined in the previous section to three zero-offset synthetic data sets. These data sets were modeled assuming reflectivity models of increasing complexity. The range of reflector curvature progressively increases from the first model to the third model.

Figure 1 shows the reflectors geometry used to model the three synthetic data sets. I modeled the first data set assuming a "cloud"of 46 point diffractors (panel a). For the second data set, I added eight curved reflectors with positive radius of curvature of approximately 55 meters (panel b). Finally, for the third data set, I added eight additional curved reflectors with a negative radius of curvature of approximately 55 meters (panel c). I set the maximum amplitude of the curved reflectors to be about 40% of the maximum amplitude of the point diffractors to maintain a balance between the velocity information provided by the point diffractors and that provided by the curved reflectors.

All the figures in this section follow the same pattern established in Figure 1. The left panels correspond to the reflectivity model shown in Figure 1a, the middle panels correspond to the reflectivity model shown in Figure 1b, and the right panels correspond to the reflectivity model shown in Figure 1c.

Figure 2 shows the three data sets modeled from the reflectivity models shown in Figure 1 assuming constant velocity equal to 2 km/s. The data increases in complexity and the texture changes as the curved reflectors are added to the reflectivity model.

Figure 3 shows the migrated sections obtained with the initial (too low) velocity of 1.951 km/s. The crossing of events in these images clearly indicates undermigration. The events corresponding to the reflectors with negative curvature are sufficiently undermigrated that they appear as reflectors with high positive curvature.

Figure 4 shows the results of the focusing analysis on the residual migrated ensembles obtained from the undermigrated images shown in Figure 3. All three panels show the image-focusing semblance spatially averaged in analysis windows defined

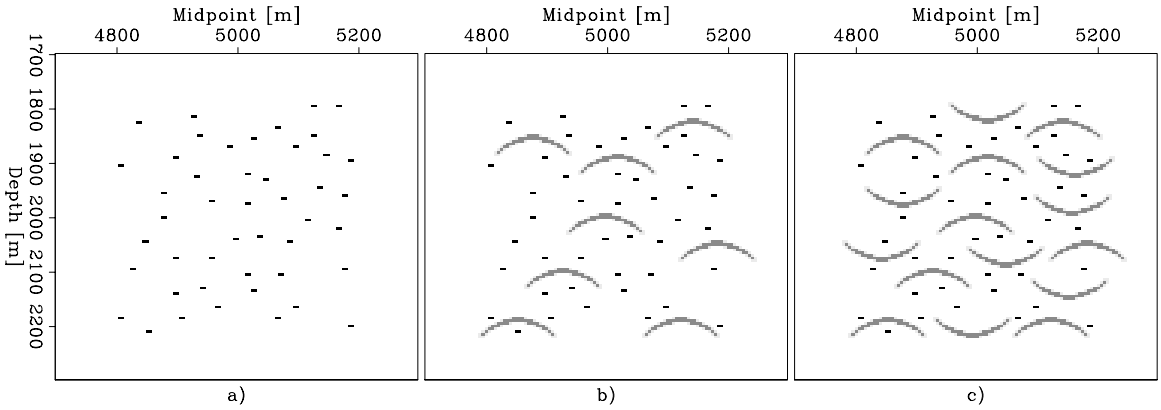

Figure 1: Reflectors geometry used to model the three zero-offset synthetic data sets I used to test the proposed image-focusing velocity-estimation method: (a) a "cloud" of point diffractors, (b) point diffractors and curved reflectors with positive curvature, (c) point diffractors, curved reflectors with positive curvature, and curved reflectors with negative curvature. [**ER**]

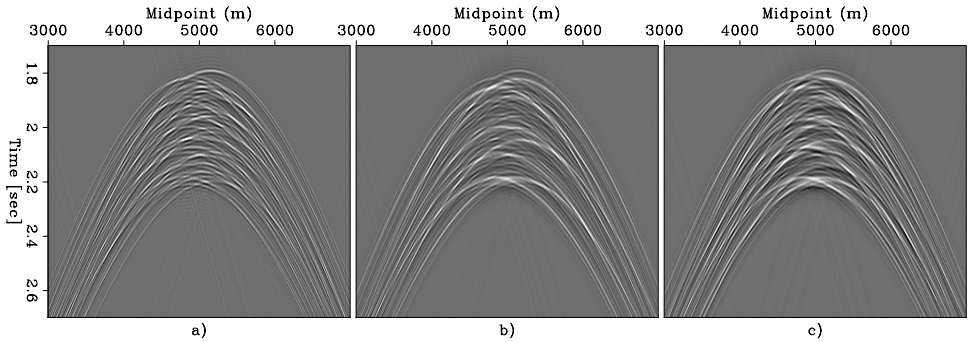

Figure 2: Zero-offset data modeled from the reflectivity functions shown in Figure 1. [**ER**]

by the following inequalities along the depth axis: 1.8 km $\leq$z$\leq$ 2.1 km, and by the following inequalities along the midpoint axis: 4.85 km $\leq$x$\leq$ 5.15 km. These analysis windows are represented in Figure 3 by the inner squares delimited by the grid superimposed onto the images. The panels show the average semblance as a function of the velocity parameter ρ and the radius of curvature R.

The semblance panels show diagonal trends for all cases because of the velocity/curvature ambiguity. When only point diffractors are present, only one trend is visible and the pattern is symmetric around ρ=1.025; that is, the correct value of the parameter. The addition of the positive-curvature reflectors adds another trend to the semblance panel (Figure 4b) and breaks downs the symmetry. When reflectors with both negative and positive curvature are present (Figure 4c), the semblance maxima occur around the correct value (ρ=1.025) for all the trends in the panel.

In poorly focused images corresponding to ρ values both lower and higher than the

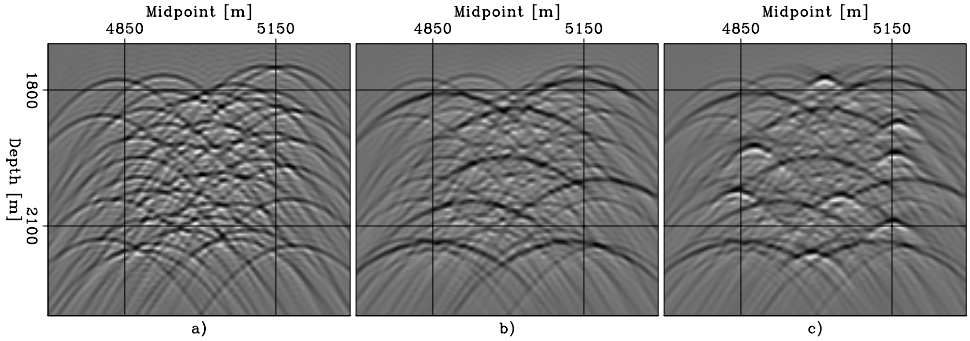

Figure 3: Migrated sections obtained by migrating the data shown in 2 with the initial (too low) velocity of 1.950 km/s. The inner squares delimited by the grid superimposed onto the images show the analysis windows, where the semblance is spatially averaged to produce the results shown in Figure 4. [**ER**]

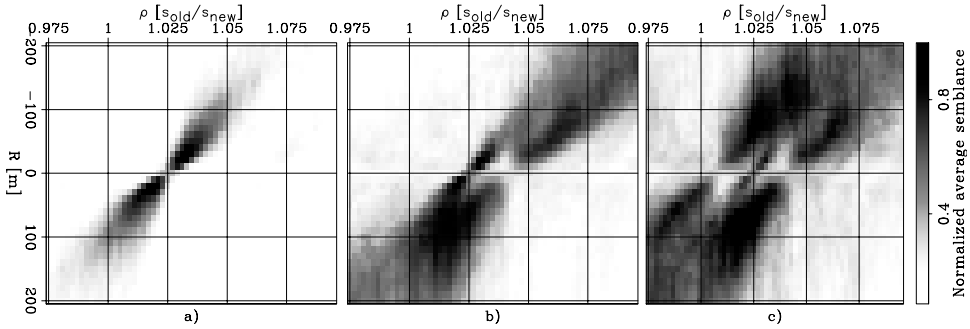

Figure 4: The image-focusing semblance spatially averaged over the analysis windows shown as a function of velocity parameter ρ and the radius of curvature R. Panel (a) shows the result corresponding to the point diffractors, panel (b) shows the result corresponding to the point diffractors and curved reflectors with positive curvature, and panel (c) shows the result corresponding to point diffractors, curved reflectors with positive curvature, and curved reflectors with negative curvature. [**CR**]

correct one, the increase in range of reflector curvatures causes additional crossing events. These crossing events interfere with the local dip estimation (step 2) and consequently with the curvature correction (step 4) Biondi (2009). As a result, the image-focusing semblance that measures dip coherency after the curvature correction is strongly attenuated for poorly focused images.

NEW YORK HARBOR DATA EXAMPLE

I tested the method for extracting velocity information from zero-offset data on a shallow seismic data set acquired in New York harbor using a 512i sub-bottom profiler with a 1-10 kHz pulse (Schock et al., 1989, 1994). Compared with conventional exploration data, these data contain much higher frequencies (useful signal is up to

about 2,000 Hz) and have been acquired with correspondingly dense, though quite irregular, spatial sampling. For the sake of simplicity, I assumed that the acquisition grid was regular with spatial sampling of 0.225 meters; that is, the average of the actual sampling for the subset I analyzed. The actual standard deviation of the spatial sampling is about 0.018 meters; that is, about 8%.

Figure 5 shows the subset of the data that I worked with. The water bottom primary reflection is recorded at about 18 milliseconds; strong multiple reflections are visible below the primaries. From nearby well-boring, the layered body in the middle is thought to be composed by Holocene sediments, mostly sands, with velocity of approximately 2.150 km/s. The sediments are surrounded by serpentinite that has much higher seismic velocity. The serpentinite velocity ranges from 2.500 km/s where the rock is fractured (on the left of the sediments) to 4.300 km/s, where the rock is intact (below the sediments).

I first migrated the data assuming a constant velocity equal to the velocity of water; that is, 1.500 km/s. Figure 6 shows the depth-migrated section. The diffraction-like events visible in the data just after the water-bottom reflection are properly focused in the migrated section. The deeper events show some sign of undermigration, but it is difficult to judge with certainty.

I performed the focusing analysis described earlier in the paper on a small analysis window; this window was centered on the events at flattish sediment-serpentinite interface at the bottom of the sediment layers. The depth of the analysis window ranged from 21 to 25 meters, for the first iteration. I adjusted the depth for the following iterations to ensure that the analysis windows consistently included the same reflectors across iterations. To avoid artifacts caused by the noisy traces clearly visible in the data around the midpoint location of 126 meters, I further limited the analysis window horizontally, to span only the midpoint interval between 87 to 126 meters.

Figure 7 shows the image-focusing semblance averaged in the analysis window as a function of the velocity parameter ρ and the radius of curvature R. There are two distinguishable trends in this semblance plot. The strongest trend corresponds to reflectors with positive radius of curvature between 2 and 5 meters. A much weaker trend corresponds to reflectors with curvature of similar magnitude, but negative. The semblance global maximum can be found at ρ=1.225 and R=4 meters. It is thus reasonable to assume that the majority of reflectors have positive curvature and a small fraction have negative curvature. Consequently, I used the value of ρ corresponding to the semblance global maximum to update the interval velocity for the sediments. Notice that if the curved reflectors from the strongest trend were assumed to be diffractors (R=0), the corresponding estimated residual-migration parameter ρ would be approximately 1.3, which is clearly too high.

To update the velocity in the sediments from the picked ρ value I followed conventional migration velocity analysis procedure for vertical velocity updating (Biondi, 2006). I assumed constant velocity in the sediment layer and estimated the updated

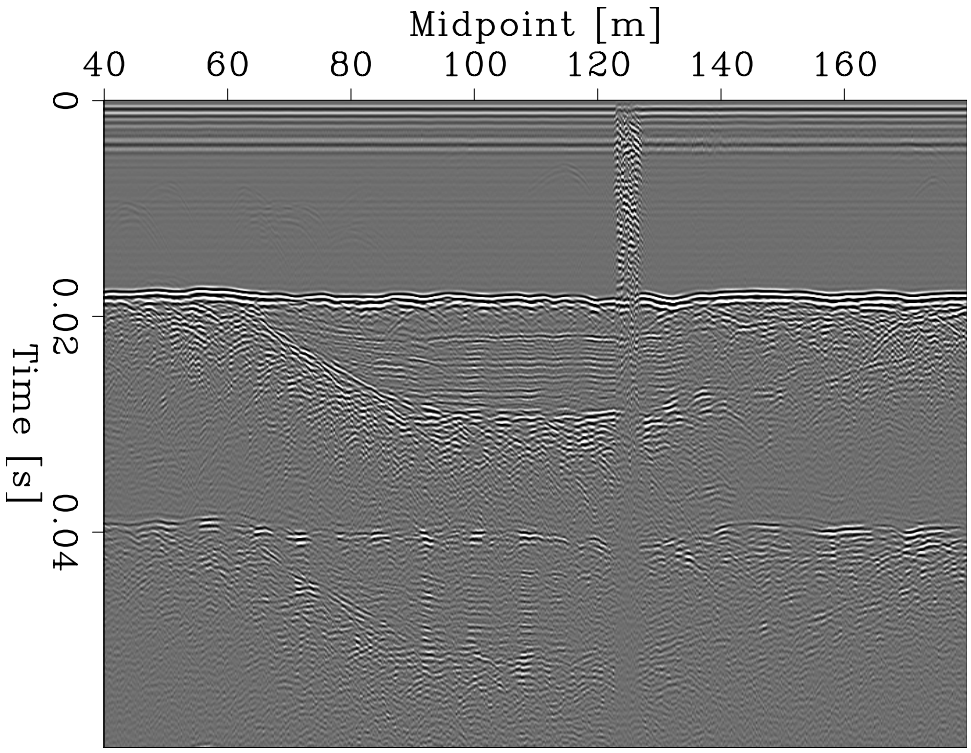

Figure 5: Zero-offset data recorded in New York harbor using a 512i sub-bottom profiler with a 1-10 kHz pulse. [**CR**]

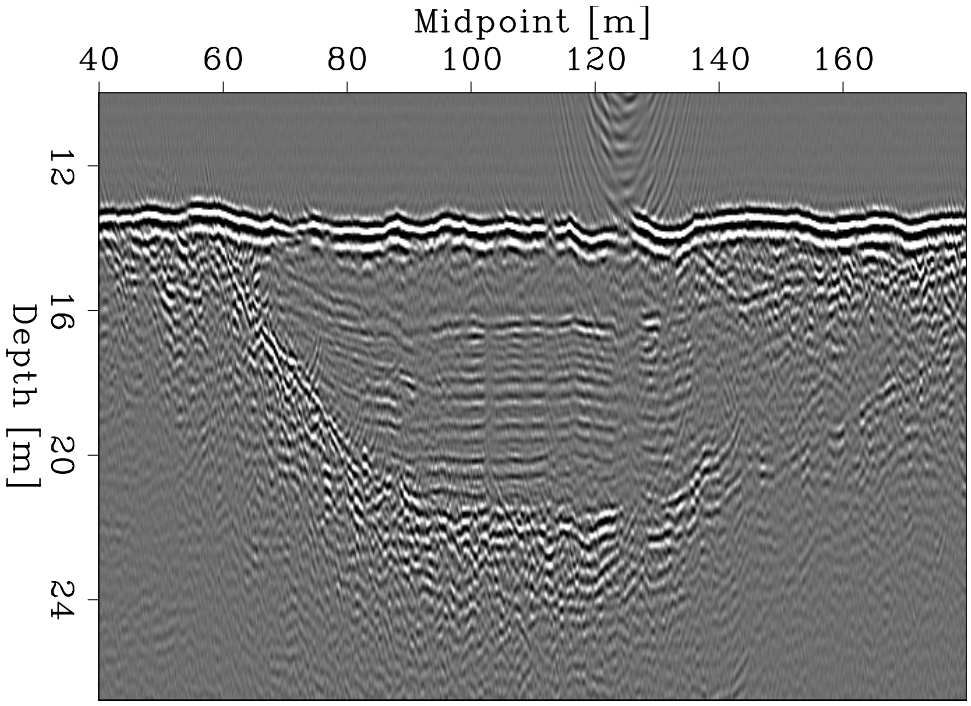

Figure 6: Depth-migrated section obtained assuming a constant velocity equal to the velocity of water; that is, 1.500 km/s. [**CR**]

velocity in the sediments $\widehat{V}_s$ by applying the following equation:

$$\widehat{V}_s = \sqrt{\frac{(\rho^2 - 1)\, V_w^2 \Delta t_w + \rho^2 V_s^2 \Delta t_s}{\Delta t_s}}, \tag{2}$$

where V_w is water velocity, V_s is the current estimate of sediment velocity, Δt_w is two-way traveltime in the water layer, and Δt_s is two-way traveltime in the sediments. At the first iteration V_s is set to water velocity. I picked the values of the traveltime intervals from the section displayed in Figure 5 and set Δt_w=.018 s and Δt_s=.012 s. Entering these values and ρ=1.225 into equation 2 results into $\widehat{V}_s$=2.250 km/s.

This velocity is slightly higher than the final one because of the limitation of the linearized residual migration I used. For large velocity errors, this residual migration undercorrects the image because it does not take into account ray bending. The error encountered in this case is larger than 20%. Consequently, the residual-migration parameter ρ is overestimated. However, another iteration of the velocity updating is sufficient to converge. My conjecture about the cause of the velocity-correction overshooting is supported by Figure 12, as discussed below.

The two panels in Figure 8 show respectively the result of the focusing analysis after migrating the data with the intermediate velocity function, V_s=2.250 km/s (panel a), and the final velocity function, V_s=2.155 km/s (panel b). This final velocity for the sediments was estimated using equation 2 with ρ=0.975; that is, the ρ value that corresponds to the maximum in Figure 8a. The semblance peak in Figure 8b occurs at ρ=1, indicating that the process has converged. The estimated value of 2.155 km/s for the sediment velocity is consistent with the geologic information available from well drilled near the location where the data were acquired.

Figure 9 summarizes the iterative velocity-estimation process by showing the velocities as a function of depth at each iteration. The solid line (labeled as "Initial") represents the starting velocity, constant and equal to water velocity. The dashed line (labeled as "Intermediate") represents the result of the first correction, which slightly overshoots. The dotted line (labeled as "Final") represents the final velocity function.

Figure 10 compares the images obtained with the three velocities in the analysis window. Figure 10a shows a zoom into the image shown in Figure 6. Figure 10b shows a zoom into the migrated image obtained using the overcorrected velocity function, and Figure 10c shows the final image. Compared with the other two images, the final image shows substantial improvement in the continuity of the reflectors and a reduction in the amount of crossing events.

Figure 11 compares the entire image obtained with the initial velocity (top panel) with the entire image obtained with the final velocity (bottom panel). The improvement in the image are substantial also outside of the analysis window. The image for the dipping interface between the sediments and serpentinite at the left of the analysis window (between 60 and 90 meters along the midpoint axis) is more continuous

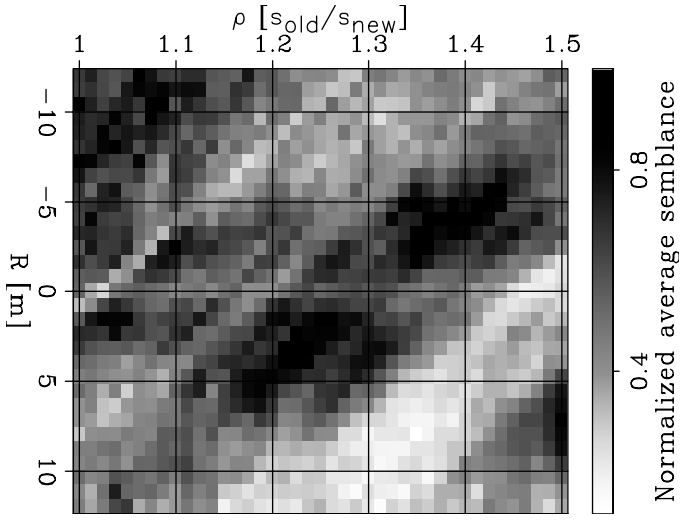

Figure 7: Image-focusing semblance computed from the initial migrated section and spatially averaged over the analysis window. Figure 6. [**CR**]

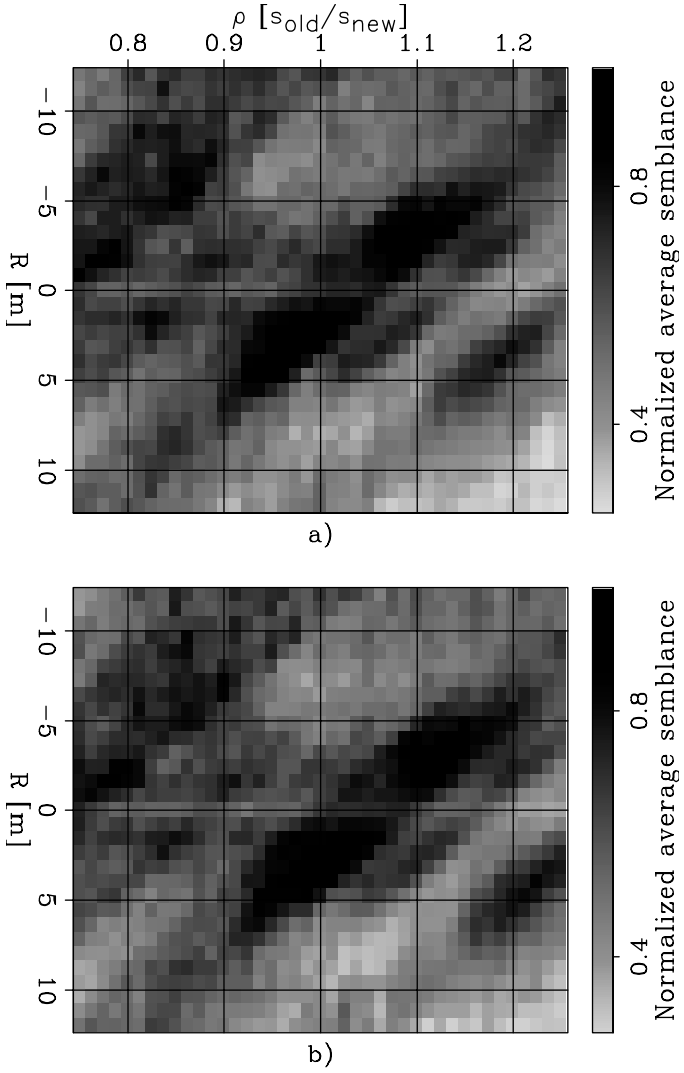

Figure 8: Image-focusing semblance computed from: (a) the intermediate migrated section, and (b) the final migrated section. [**CR**]

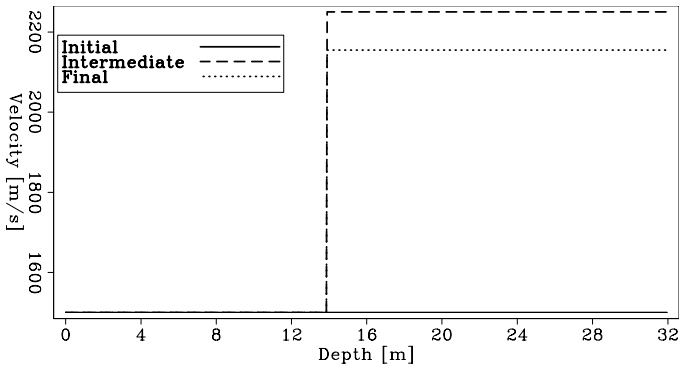

Figure 9: Velocity functions used for the three iterations of velocity-estimation process. [**ER**]

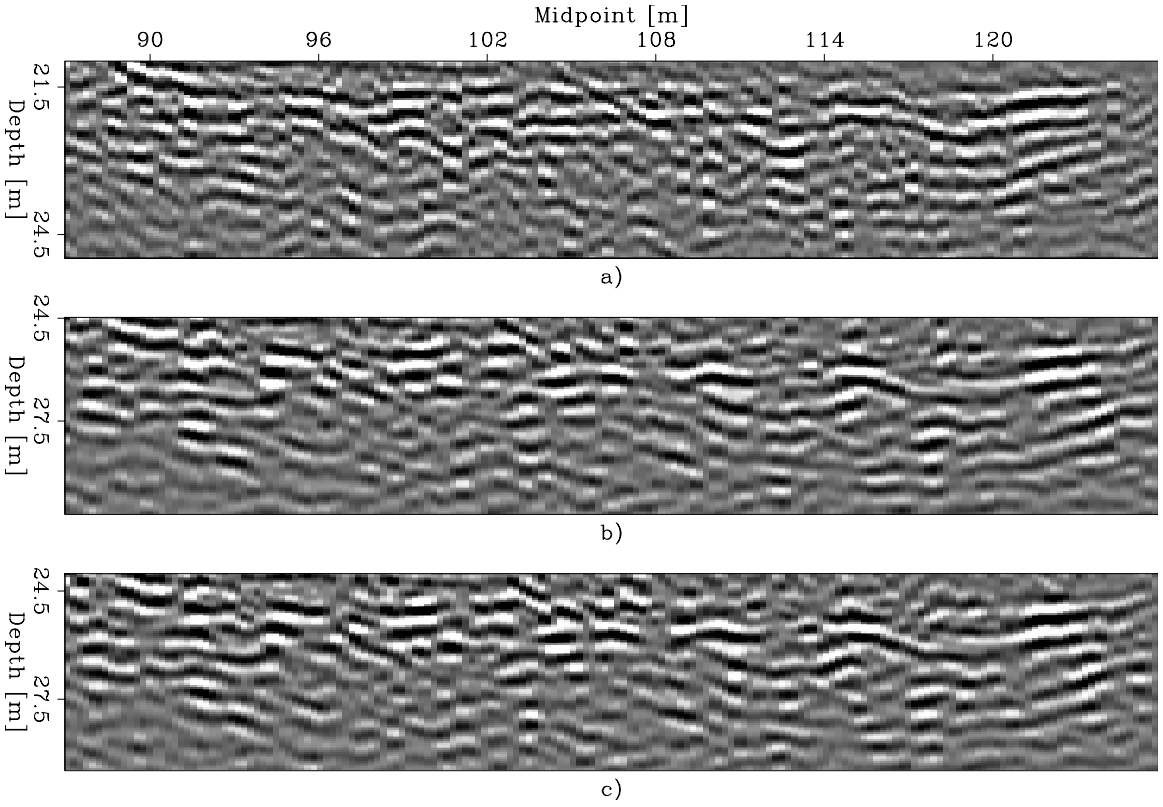

Figure 10: Migrated images in the analysis window for the three iterations: (a) initial velocity, (b) intermediate velocity, and (c) final velocity. [**CR**]

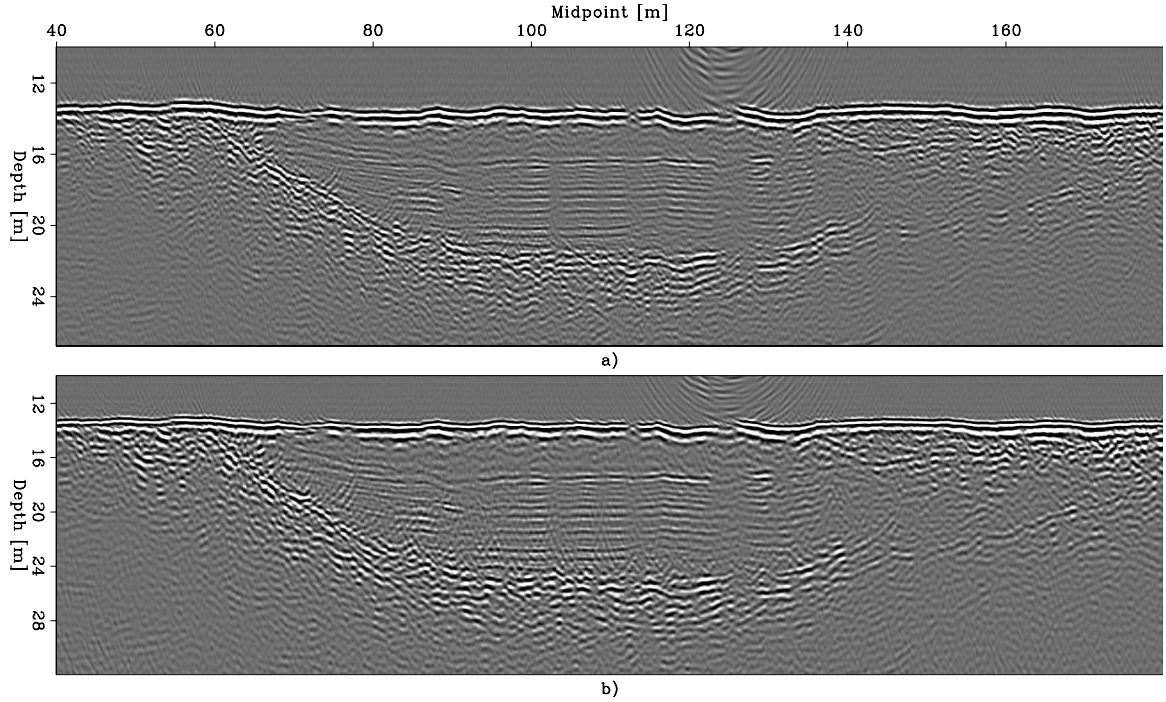

Figure 11: Comparison of the entire images obtained with: (a) initial velocity, and (b) final velocity. [**CR**]

in the final than in the initial image. The reflections just below this interface are also better focused in Figure 11b than in Figure 11a. Similarly, the reflector at the bottom of the sediment layer on the right of the analysis window (between 140 and 160 meters along the midpoint axis) is more continuous in the final image than in the initial one.

Finally, Figure 12 supports my previous conjecture that the overestimation of the velocity correction at the first iteration is caused by accuracy limitations of the linearized residual migration I employed when correcting for large velocity errors. This figure compares the analysis window for the final migrated image (top panel) with the analysis window taken from the residual migration of the first migrated image that corresponds to the picked value of ρ; that is, with $\rho = 1.225$ (bottom panel). These two images are very similar, demonstrating that the first ρ estimate is consistent with the final, and "optimal", velocity estimate. It leads to overshooting the interval-velocity correction because the residual migration is inaccurate. Notice that the differences in the vertical axis between the two sections are caused by the remapping to pseudo-depth of the residual-migrated section shown in Figure 12b.

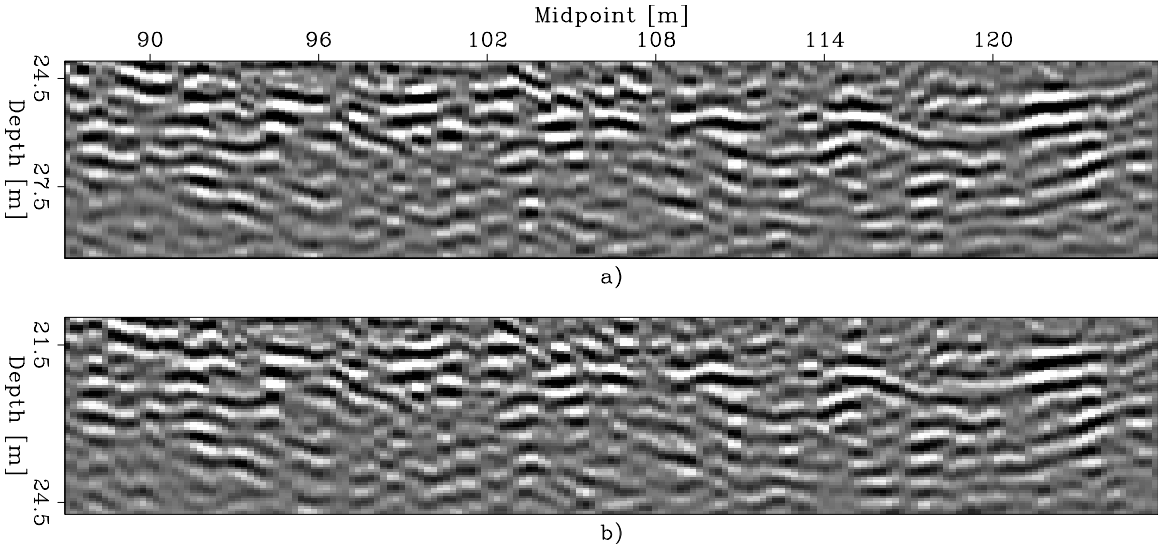

Figure 12: Comparison of the migrated images in the analysis window for (a) final velocity, (b) residual migration of the starting image for ρ=1.225. The image-focusing method selected the bottom image to be the best focused image among the ensemble of residual migrated images obtained from the initial migration. [**CR**]

CONCLUSIONS

Velocity information can be successfully extracted from zero-offset data by analyzing focusing and defocusing of residual-migrated images. The results shown in this paper demonstrate that the estimation method I presented in Biondi (2009) provides quantitative information on velocity without relying on subjective interpretative criteria.

The synthetic examples illustrate how the resolution and reliability of the velocity estimates increase when the target contains reflectors with a broad range of curvatures. This insight is useful to guide the application of the suggested method to practical problems.

The New York harbor example shows that the proposed method is sufficiently robust to provide reliable and quantitative velocity information from field data. The estimated interval velocity function is consistent with available geologic information and improves the focusing of the image both in the analysis window and outside the analysis window.

ACKNOWLEDGMENTS

I would like to thank the United States Army Corps of Engineers (USACE) New York District and Earthworks under contract number W912DS-06-D-0001 for providing the field data. I would also to acknowledge Daniel Rosales with Earthworks for his enthusiastic help in providing the data to SEP.

REFERENCES

Biondi, B., 2006, 3D Seismic Imaging: Society of Exploration Geophysicists.

———, 2008, An image-focusing semblance functional for velocity analysis: SEP-Report, **136**, 43–54.

———, 2009, Measuring image focusing for velocity analysis: SEP-Report, **138**, 59–79.

Fomel, S., 2002, Applications of plane-wave destruction filters: Geophysics, **67**, 1946–1960.

Sava, P., 2004, Migration and velocity analysis by wavefield extrapolation: PhD thesis, Stanford University.

Sava, P. C., 2003, Prestack residual migration in frequency domain: Geophysics, **68**, 634–640.

Schock, S. G., L. R. LeBlanc, and L. A. Mayer, 1989, Chirp subbottom profiler for quantitative sediment analysis: Geophysics, **54**, 445–450.

Schock, S. G., L. R. LeBlanc, and S. A. Panda, 1994, Spatial and temporal pulse design considerations for a marine sediment classification sonar: IEEE Journal of Oceanic Engineering, **19**, 406–415.